Front. Earth Sci. 2020, 14(1): 236–250
https://doi.org/10.1007/s11707-019-0749-9

RESEARCH ARTICLE

Simulation of Moon-based Earth observation optical image processing methods for global change study

Tong LI (✉)[1,2], Huadong GUO[1], Li ZHANG[1], Chenwei NIE[1,2], Jingjuan LIAO[1], Guang LIU[1]

1 Key Laboratory of Digital Earth Science, Institute of Remote Sensing and Digital Earth, Chinese Academy of Sciences, Beijing 100094, China
2 University of Chinese Academy of Sciences, Beijing 100049, China

Abstract Global change affected by multiple factors, the consequences of which continue to be far-reaching, has the characteristics of large spatial scale and long-time scale. The demand for Earth observation technology has been increasing for large-scale simultaneous observations and stable global observation over the long-term. A Moon-based observation platform, which uses sensors on the nearside lunar surface, is considered a reasonable solution. However, owing to a lack of appropriate processing methods for optical sensor data, global change study using this platform is not sufficient. This paper proposes two optical sensor imaging processing methods for the Moon-based platform: area imaging processing method (AIPM) and global imaging processing method (GIPM), primarily considering global change characteristics, optical sensor performance, and motion law of the Moon-based platform. First, the study proposes a simulation theory which includes the construction of a Moon–Sun elevation angle model and a global image mosaicking method. Then, coverage images of both image processing methods are simulated, and their features are quantitatively analyzed. Finally, potential applications are discussed. Results show that AIPM, whose coverage is mainly affected by lunar revolution, is approximately between 0% and 50% with a period of 29.5 days, which can help the study of large-scale instant change phenomena. GIPM, whose coverage is affected by Earth revolution, is conducive to the study of long term global-scale phenomena because of its sustained stable observation from 67°N–67°S on the Earth. AIPM and GIPM have great advantages in Earth observation of tripolar regions. The existence of top of the atmosphere (TOA) albedo balance line is verified from the GIPM perspective. These two imaging methods play a significant role in linking observations acquired from the Moon-based platform to Earth large-scale geoscience phenomena, and thus lay a foundation for using this platform to capture global environmental changes and new discoveries.

Keywords Moon-based Earth observation, optical imaging processing method, global change, remote sensing, simulation

1 Introduction

Placing sensors on the near-side of the Moon to form a Moon-based observation platform for observing the Earth is regarded as an ideal Earth observation method that is capable of monitoring global change (Karalidi et al., 2012; Guo et al., 2014). Compared with existing observation systems, the Moon-based platform has advantages such as (Guo et al., 2018): 1) Longevity. As the only natural satellite, the Moon will always be there with a regular rotation and orbit. 2) Integrity. To view the whole Earth disk from the Moon at any given time, a field angle of view of approximately 2° is needed. 3) Stability. Few moonquake activities occur on the Moon.

After consideration of several options, optical sensors that have been commonly used in Earth observation are considered to be a practicable choice for a Moon-based platform. Established optical sensors on a Moon-based platform can obtain more wider continuous observational data than many existing earth observation systems (Ren et al., 2017). Optical sensor on the Moon-based platform can cover approximately one hemisphere of the earth with a small field of view (about 2°), because the distance between Earth and the Moon is much larger than the radius of Earth (Ye et al., 2017). The spatial resolution and temporal resolution of an optical sensor can reach 1 kilometer (Ding et al., 2014) and 20 min (Liu et al., 2016), respectively, which is reasonably enough for the study of large-scale geoscience phenomenon.

The history of Earth observation through optical sensors from the Moon could date back to the 1960s. Apollo 16

Received October 23, 2018; accepted February 28, 2019

E-mail: litong2016@radi.ac.cn

(Carruthers and Page, 1972) astronauts used a far-ultraviolet camera/spectrograph to obtain images and spectra of Earth's atmosphere. Later, Pallé and Goode (2009) researched Earth's albedo through light reflecting to the lunar surface. Huang (2008) simulated monitoring the Earth energy balance via the Moon-based platform and found that the acquired observation data could make up for a deficit of satellite data. Recently, Chinese scientist Huadong Guo (2009) formalized the scientific concept of the Moon-based Earth observation platform. Guo et al. (2014) comprehensively analyzed its characteristics and potential applications and pointed out that the Moon-based platform should be mainly used for observation of the large-scale geoscience phenomena on Earth. This platform has been investigated by several researchers in different branches. Zhang (2012) used the Jet Propulsion Laboratory (JPL) ephemerides to study Moon-based observation Earth simulation technology. Guo et al. (2018) studied characteristics and performance of a synthetic aperture radar (SAR) on the Moon-based platform. Ren et al. (2017) and Ye et al. (2017, 2018) built a geometric model of the Moon-based platform to investigate a Moon-based optical sensor's observational performance. Xu and Chen (2018) developed a Moon-based SAR theory and found that the Moon revolution and the error that is caused by the 'stop-and-go' assumption are potentially significant to the Doppler parameters. The commonalities of these studies focus on objective facts such as geometric relationships of the Moon-based platform to certify its characteristics compared with other observation systems. However, how to apply the Moon-based observation method to the study of large-scale geoscience phenomena on Earth is, until now, unclear owing to a lack of in-depth analysis of the Moon-based optical sensor's imaging capability. Therefore, it is important to study methods applied to form observational images.

This study strives to propose two imaging processing methods for a Moon-based optical sensor by considering global change characteristics, optical sensor performance, and the motion law of the Moon-based platform. The Moon–Sun elevation angle model and the Moon-based global image mosaicking method have been created as two key methods for simulating observation cover area to analyze the performance of proposed methods. This study simulates coverage images based on two key methods and analyzed their performance. Meanwhile, links between two methods and their potential applications have been discussed. The methods proposed in this paper can promote global change study using the Moon-based platform. The two key methods can be used in simulating the Moon-based observation data and are of great significance to the design of a Moon-based optical sensor in the future.

In the next section of this paper, two imaging processing methods of the Moon-based platform's optical sensors are proposed, and their features are described. A simulation theory including the Moon–Sun elevation angle model and the global image mosaic method is introduced in Section 3. Two imaging processing method characteristics are shown through quantitative analysis in Section 4. In Section 5, effectiveness of global image mosaicking method, the inherent relation of area imaging processing method (AIPM) and global imaging processing method (GIPM), and their potential applications are discussed. Finally, conclusions are drawn in Section 6.

2 Imaging processing methods of Moon-based optical sensor

An imaging processing method is a process of forming an image based on geographic coordinate information according to an optical sensor on the Moon-based platform. A Moon-based optical sensor's imaging processing method set depends on individual research demand unlike the satellite observational method which obtains photoelectric signals by optical sensors in different imaging technology such as staring imaging (Cui et al., 2017) and push-broom imaging (Mouroulis et al., 2000). Moon-based observational images are generated by imaging processing method under consideration to global changes' characteristics, optical sensor's performance, and the motion law of the Moon-based platform.

Characteristics of global change have been well summarized with ongoing research as two main aspects. (Wu, 1999; Wild, 2009; Zhu et al., 2012; Guo and Zhu, 2013). The spatial-scale and temporal-scale of global change are directly proportional. Specifically, global-scale phenomena are changing slowly. Meanwhile, numerous large-scale cross-complex geoscience phenomena under cross-coupling effect accelerate occurrence of larger-scale, even global-scale, geoscience phenomena. Some of factors caused global change are characterized by transient and large-scale change, which require a wide range observation. Therefore, Earth observation technology should have features including large cover range, good coverage, and continuous observation (Chuvieco et al., 2010; Butler, 2014; Guo et al., 2014). Accordingly, optical imaging processing method for the Moon-based platform should meet the needs of Earth observation technology.

Figure 1, a simplified Sun–Moon–Earth rotation model, shows the Moon-based optical sensor's observing area. As the Earth spins each day with a larger speed than the Moon's orbit around the Earth, the observing area will cover around the Earth.

Based on the above analysis, the Area Imaging Processing Method (AIPM) is defined as an imaging method using instantaneous observational data to generate wide-disk images and Global Imaging Processing Method (GIPM) as an imaging method using accumulated

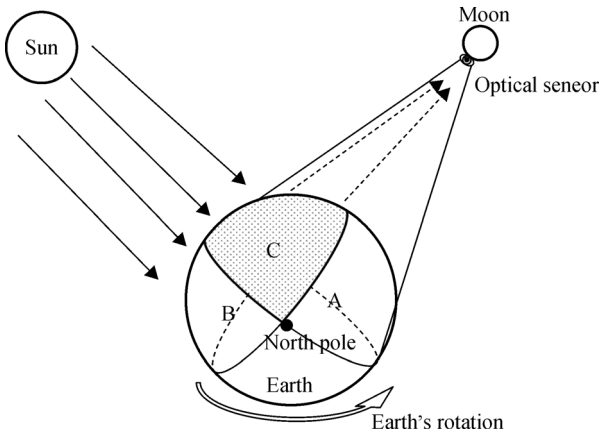

Fig. 1 Sun-Earth-Moon rotation system. Regions B and C represent sunlit area. Region A and C are the observing area of the Moon-based optical sensor, which is approximately a hemisphere. Thus, the intersection region C represents the observational area by the Moon-based optical sensor.

observational data within a single day to generate a global-range image. GIPM can be regarded as a derivative of numerous AIPM's coverage images in application of macroscopic global change study as a whole-Earth data source. Therefore, GIPM and AIPM, with different emphasis of application fields, are proposed as two independent processing methods in this paper. AIPM and GIPM's characteristics are separately compared as follows: Cover area of AIPM varies with time, and its maximum coverage at certain times can reach up to approximately half of the Earth. AIPM obtains instantaneous changing parameters of geoscience phenomena that can be used in large-scale change research, such as Earth radiation and atmospheric change. In comparison with the variable coverage area of AIPM, GIPM's cover area, which is mosaicking of AIPM's cover area with a certain frequency, is relatively stable in an imaging time unit of a single day. GIPM is significant for global-scale geoscience phenomenon's research in a long period, such as Earth energy balance over a decade or even a century.

To quantify AIPM and GIPM's performance, we simulate their coverage images based on three assumptions:

1) The optical sensor will be installed on the center of the nearside lunar surface, which has been verified as an ideal place on the Moon surface (Ye et al., 2018).

2) Observational region is affected by lunar altitude angle (Nie et al., 2018), which needs to be combined with the actual sensor. In the simulation theory constructed in this study, the lunar altitude angle is assumed to set to 0°.

3) Despite the topographic relief and atmosphere, we assume that the Earth and the Moon mentioned in this study are ideal spheres. Owing to the large distance between the Earth and the Moon, the influence of topographic relief and atmosphere can be ignored.

3 Simulation theory

To simulate AIPM and GIPM's coverage images, we created a Moon–Sun elevation model and a global image mosaicking method. Figure 2 shows the simulation process.

3.1 Data

3.1.1 Global observation grids

To acquire a global distribution of the Moon–Sun elevation angle, we calculated the Moon–Sun elevation angle of each point on Earth, which is included in global Earth observation grids. A suitable grid resolution needed to be chosen. We divided the Earth surface into equally spaced 180×360 grids, with a grid resolution of $1° \times 1°$, and provided latitude and longitude information. Previous research showed that the resolution of a Moon-based optical sensor can reach 1 kilometer (Ding et al., 2014). Thus, setting the resolution at 1° is reasonable.

3.1.2 Experiment time

Time determines relative position of the Earth, Moon, and Sun. Reasonable experiment time should fully reflect features of two optical imaging processing methods under the consideration of relative position of the Earth, Moon, and Sun. As sunlight is the main source for optical sensors, and the Earth has a longer revolution (approximately 365 days) than that of the Moon (approximately 29 days), the experiment time we set from 00:00 on June 21, 2016 to 00:00 on December 21, 2016 in Universal Time Coordinated (UTC) matches the subsolar point moving from the tropic of Cancer to the tropic of Capricorn. Here, AIPM's coverage images are simulated per hour, with 4,416 images (184 days $\times$ 24 images/day) generated. GIPM's coverage images are simulated per day, with 184 images generated.

3.1.3 JPL ephemerides

Positions of the Earth and the Moon can be obtained by the processing of ephemeris data, which stores positions and velocities of celestial bodies at a given time. The DE430 high-precision ephemeris developed by NASA JPL is an ephemeris data source recommended by International Earth Rotation Service (IERS) (Folkner et al., 2014) and it is also commonly used in Moon-based Earth observation research (Ren et al., 2017; Ye et al., 2017, 2018). The JPL ephemerides provide planetary three-dimensional Cartesian reference data on the basis of the Earth-centered inertial coordinate system in the form of Chebyshev interpolation polynomials, which contain Chebyshev interpolation polynomial coefficients. Many researchers have expounded how to use JPL ephemeris to obtain

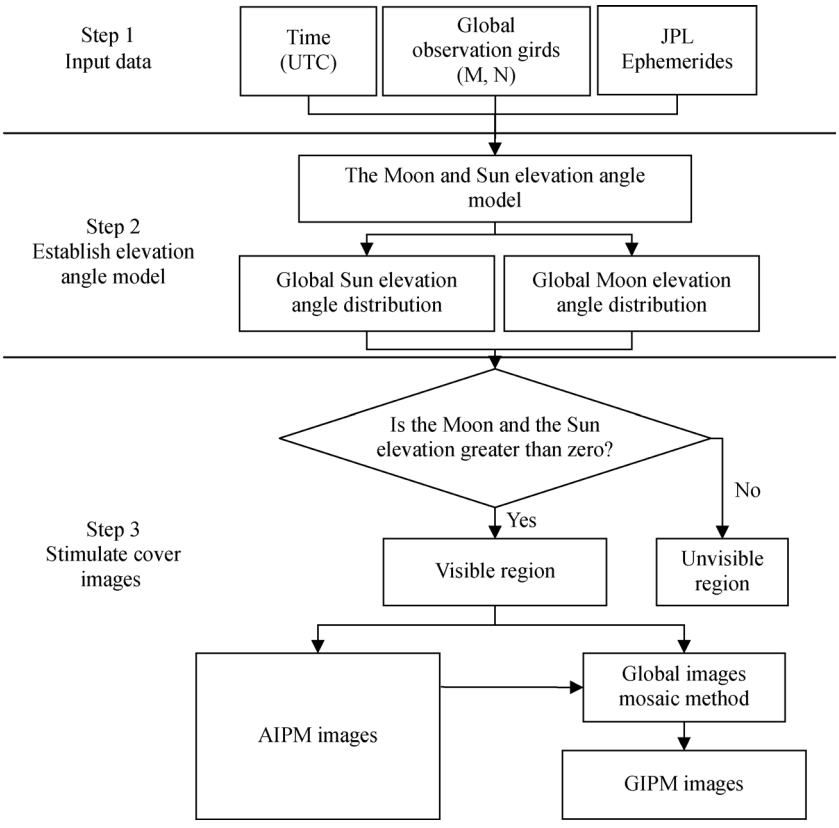

Fig. 2 Flow chart of simulated optical imaging processing methods' cover area images. The first step is to prepare input data, including parameters such as the global Earth observation grids, experiment time, and Jet Propulsion Laboratory (JPL) Ephemerides. The second step is to obtain global-sun-elevation-angle-distribution and global-Moon-elevation-angle-distribution by inserting these parameters. AIPM's cover area is the region where both elevation angles are greater than 0°. GIPM's images are obtained through the global image mosaicking method.

positions of the Moon–Sun in the geocentric reference system (Zhang, 2012; Ren et al., 2017; Ye et al., 2017, 2018). By processing DE430 ephemeris, we define both coordinates of the center of mass of the Moon and the center of mass of the Sun in Earth-centered inertial (ECI) coordinate system at time t as $(X_{mt}, Y_{mt}, Z_{mt})_{ECI}$ and $(X_{st}, Y_{st}, Z_{st})_{ECI}$, respectively, that will be used in the Moon–Sun elevation angle model.

3.2 Moon–Sun elevation angle model

The Moon–Sun elevation angle model is used to calculate elevation angle distributions of the Moon and the Sun on Earth's surface at a given time. This model takes time, global observation grids, and ephemeris data as input parameters and calculates the elevation angle distribution. The modelling procedure is shown in Fig. 3.

3.2.1 Transformations of the reference systems

Moon–Sun elevation angles must be calculated in the horizontal coordinate system. However, the Moon–Sun position is given by JPL ephemerides in the Earth-centered inertial coordinate system. Thus, the coordinates need to be transformed. Three coordinate systems are considered in the coordinate transformation.

Earth-centered inertial (ECI) coordinate system is a geocentric coordinate that does not rotate with the Earth. Its origin is at Earth's center of mass. The X–Y plane coincides with the equatorial plane of Earth. The X-axis is permanently fixed in a direction relative to the celestial sphere. The Z-axis lies at a 90° angle to the equatorial plane and extends through the North Pole; the Y-axis is determined according to the right-hand rule (Ligas and Banasik, 2011).

Earth-centered Earth-fixed (ECEF) coordinate system is also regarded as a geocentric coordinate, but it rotates with the Earth. Its origin is also defined as Earth's center of mass. The X-axis points to the intersection of the primary meridian and equator (longitude and latitude is 0°, 0°), the Z-axis points to the Earth's true north, and the Y-axis is determined according to the right-hand rule (Ligas and Banasik, 2011).

Horizontal Coordinate System (HCS) is a celestial coordinate system that uses the observer's local view (depicted in blue plane in Fig. 4) as the base plane. It is

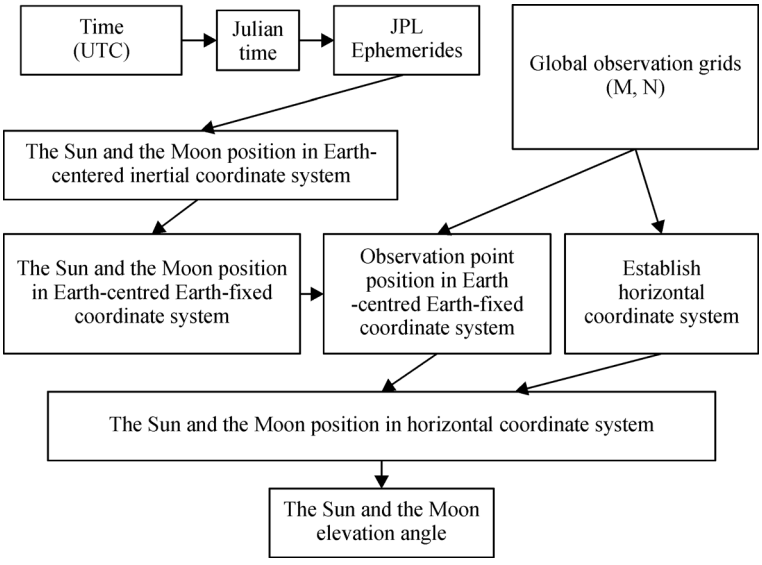

Fig. 3 Moon–Sun elevation angle model. The position of the Moon and the Sun in the Earth-centered inertial coordinate system can be looked up in JPL ephemeris data through Julian time converted from UTC. Then, the Earth-centered inertial coordinate system is converted into the Earth-centered Earth-fixed coordinate system. We establish a horizontal coordinate system based on every point which existed in a global observation grid. After that, the positions of Earth and the Moon in the Earth-centered Earth-fixed coordinate system are converted into the horizontal coordinate system and finally, elevation angles of the Sun and the Moon in the horizontal coordinate system are calculated.

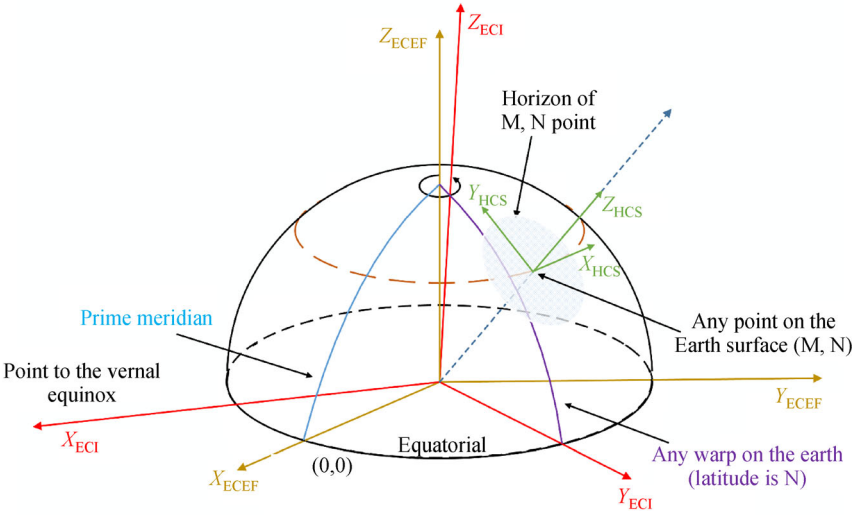

Fig. 4 Relationship of each coordinate system. Earth-centered Inertial coordinate system shown in red in this figure is used to obtain the position of the Sun and the Moon from JPL Ephemerides. Earth-centered Earth-fixed coordinate system with the orange line is used to link the Earth-centered inertial coordinate system and the horizontal coordinate system. The horizontal coordinate system depicted in green is used for elevation angle calculation.

aligned with the local horizontal plane, such that the HCS is tangent to the Earth surfaces at the observer's local point. The observer's local point is the origin of HCS, the *Y*-axis points to the north celestial pole in the direction of the local meridian, the *X*-axis points to the east and in parallel with the local latitude line, and the *Z*-axis is determined according to the right-hand rule and pointing to the zenith angle of the horizontal coordinate system (Schombert, 2011).

Transformation steps are as follows:

1) ECI to ECEF

ECEF coordinates move with Earth's rotation, unlike the ECI coordinate system. Thus, the conversion equation is as follows:

$$[\mathrm{ECEF}] = Q(t)R(t)W(t)[\mathrm{ECI}], \quad (1)$$

where t is time, while $Q(t)$, $R(t)$, and $W(t)$ are the Earth nutation and precession, denoted by rotation matrices of

the precession, rotation, and pole shift, respectively (Petit and Luzum, 2010). These Earth position parameters change dynamically with time t. Positions of the Moon and the Sun obtained by Eq. (1) in ECEF at time t are $(X_{mt}, Y_{mt}, Z_{mt})_{ECEF}$ and $(X_{st}, Y_{st}, Z_{st})_{ECEF}$, respectively.

2) Earth observation grid to ECEF

Assume that the latitude and longitude of any point i in the global Earth observation grids is (M_i, N_i). The conversion relationship (Civicioglu, 2012) is as follows:

$$\begin{bmatrix} X_i \\ Y_i \\ Z_i \end{bmatrix}_{ECEF} = \begin{bmatrix} R_E\cos(N_i)\cos(M_i) \\ R_E\cos(N_i)\sin(M_i) \\ R_E\sin(M_i) \end{bmatrix}, \quad (2)$$

where, $[X_i, Y_i, Z_i]^T_{ECEF}$ is observation point i in ECEF, and R_E is Earth's radius.

3) ECEF to HCS

The transformation from ECEF to HCS contains two steps. First, the origin is moved from the Earth's center of mass to the observation point i on the Earth surface in ECEF. Then, the coordinates are rotated around the Z-axis and the X-axis. The conversion relationship (Clarke and Roy, 2003) is as follows:

$$\begin{bmatrix} x \\ y \\ z \end{bmatrix}_{HCS} = R_x(90^\circ - N)R_z(90^\circ + M) \left(\begin{bmatrix} x \\ y \\ z \end{bmatrix}_{ECEF} - \begin{bmatrix} X_i \\ Y_i \\ Z_i \end{bmatrix}_{ECEF} \right), \quad (3)$$

where $[X_i, Y_i, Z_i]^T_{ECEF}$ obtained by Eq. (2) is the position of observation point (M_i, N_i) in ECEF coordinates, and also the origin of HCS. $[x, y, z]^T_{HCS}$ is the HCS position of the $[X, Y, Z]^T_{ECEF}$ point. R_x (90°–N) represents the coordinate rotation around the X-axis changing with the latitude. R_z (90° + M) represents the coordinate rotation around the Z-axis, which in turn changes with the longitude.

The coordinate rotation R_x (90°–N) is given as follows:

$$R_x(90^\circ - N) : \begin{pmatrix} 1 & 0 & 0 \\ 0 & \cos(90^\circ - N) & \sin(90^\circ - N) \\ 0 & -\sin(90^\circ - N) & \cos(90^\circ - N) \end{pmatrix}. \quad (4)$$

The coordinate rotation R_z(90°+ M) is given as follows:

$$R_z(90^\circ + M) : \begin{pmatrix} \cos(90^\circ + M) & \sin(90^\circ + M) & 0 \\ -\sin(90^\circ - M) & \cos(90^\circ + M) & 0 \\ 0 & 0 & 1 \end{pmatrix}. \quad (5)$$

By inserting Eq. (4) and Eq. (5) into Eq. (3), the conversion formula is given as follows:

$$\begin{bmatrix} x \\ y \\ z \end{bmatrix}_{HCS} = \begin{bmatrix} -\sin M & \cos M & 0 \\ -\sin N\cos M & -\sin N\sin M & \cos N \\ \cos N\cos M & \cos N\sin M & \sin N \end{bmatrix} \cdot \left(\begin{bmatrix} x \\ y \\ z \end{bmatrix}_{ECEF} - \begin{bmatrix} X_i \\ Y_i \\ Z_i \end{bmatrix}_{ECEF} \right). \quad (6)$$

By inserting positions of the Moon and the Sun in ECEF coordinates into Eq. (6), positions of the Sun and the Moon in HCS are obtained as $(x_{st}, y_{st}, z_{st})^T_{HCS}$ and $(x_{mt}, y_{mt}, z_{mt})^T_{HCS}$, respectively.

3.2.2 Elevation angles and simulation of coverage images

The HCS is a type of Cartesian Coordinate System (CCS). In CCS, the elevation angle EL is given by the following equation:

$$EL = \arctan\left(\frac{S_z}{\sqrt{S_x^2 + S_y^2}} \right), \quad (7)$$

where S_x, S_y, S_z represent observed celestial bodies' positions in HCS. By inserting the Moon–Sun HCS values $(x_{st}, y_{st}, z_{st})^T_{HCS}$ and $(x_{mt}, y_{mt}, z_{mt})^T_{HCS}$ into Eq. (7), the elevation angles are obtained as EL_{Sun} and EL_{Moon}, respectively.

By calculating EL_{Sun} and EL_{Moon} for each point in the global observation grids, we mark all points with *Els* greater than zero as "1", and the rest as "0". Sequentially, a Boolean image represented AIPM's coverage image is generated.

3.3 Global image mosaicking method

GIPM's coverage images consist of AIPM's images spliced with certain imaging frequencies over one day. Setting imaging frequency appears particularly important as AIPM's coverage area varies with time (this conclusion will be drawn in Section 4.1). If the imaging frequency is set on a low level, GIPM's coverage images will not cover the whole area of the Earth, because AIPM's coverage is closest to 0% at a certain moment. Otherwise, if the imaging frequency is set on a high level, the resolution of obtained images will be reduced because it is restricted by the interaction of imaging frequency and its resolution (Tsukamoto et al., 1996). Therefore, a rational design for imaging frequency is a central task to form GIPM's coverage images.

Latitudinal positions of AIPM's coverage area move in short spurts northwards or southwards most of a day (this conclusion will also be drawn in Section 4.1). This indicates that the extent of AIPM's coverage region is

stable within one day. Based on that, GIPM's latitudinal extent accumulated by numerous AIPM-images is relatively stable. Therefore, AIPM's coverage images at the beginning of each day (00:00), can be used as the start-image to calculate GIPM's imaging frequency. Radial coverage, the cover range between east longitude and west longitude, is different at different latitudes. To ensure a GIPM's coverage image covers the whole Earth, we use AIPM's minimum radial range to calculate GIPM's imaging frequency f using the following formula:

$$f = \frac{N_{\text{radial}}}{\min\{\text{AIPM}_{\text{radial coverage}}\}}, \tag{8}$$

where N_{radial} is the number of zonal pixels in the global Earth observation grids. According to Section 3.1.1, N_{radial} is 360 in this study. $\min\{\text{AIPM}_{\text{radial coverage}}\}$ is the number of pixels at the minimum radial range of AIPM's coverage image.

We put imaging time calculated by f into the Moon–Sun elevation model to obtain AIPM's coverage images over one day. By superimposing these images, a Boolean image represented GIPM's coverage image is generated, and we obtain a GIPM's coverage image.

3.4 Spatial coverage calculation

The coverage C is calculated by the following formula:

$$C = \frac{S_{\text{m}}}{S_{\text{global}}} \times 100\%, \tag{9}$$

where S_{m} is the sum of the Boolean matrix that represents simulation coverage images which is expressed as S_{AIPM} or S_{GIPM} in this study. S_{global} represents the total number of global observation grids.

4 Results and analysis

This session tries to analyze AIPM and GIPM's coverage ability from the perspectives of spatial coverage and cover area.

4.1 Coverage ability of AIPM

Spatial coverage of all simulated AIPM's coverage images calculated by Eq. (9) on a variation curve can be seen in Fig. 5.

The results show that the spatial coverage variation of AIPM's images periodically varies, indicating an average period of 29 days and 14.8 hours, which approximately concurs with the Moon's revolution period (synodic month, 29.53 days). Therefore, we can infer that AIPM's coverage is mainly affected by the Moon's revolution. Within the simulation time span, there are six complete periods with a maximum coverage of approximately 50%, and a minimum coverage of approximately 0%. Therefore, the AIPM can cover the whole hemisphere of the Earth at once, at a certain time.

An optical sensor's maximum observational range reflects its best performance. We select six moments when AIPM's coverage reaches its maximum value to map AIPM's coverage images in the Mercator projection coordinate system. To study the variation rule of the AIPM's coverage images, we also selected two adjacent moments of the moment with maximum coverage to form

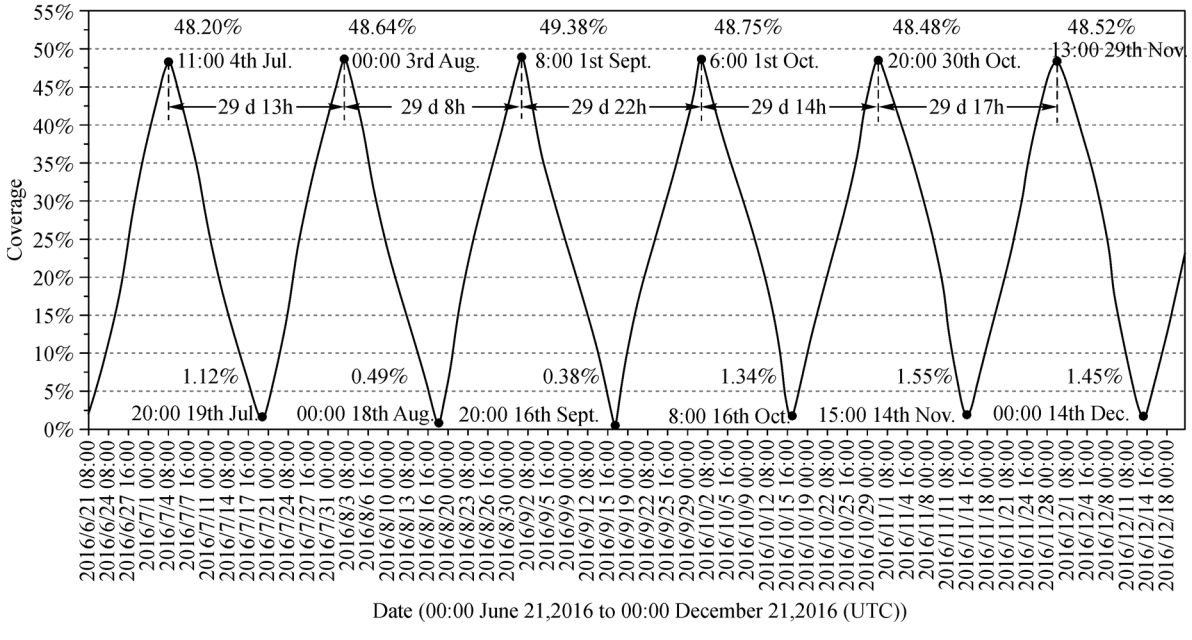

Fig. 5 Hourly AIPM's coverage in experiment time. The font on the top of this figure depicts maximum coverage of each period, and the font on the bottom of this figure depicts the minimum coverage of each period.

three AIPM's coverage images in the same picture. The result is shown in Fig. 6.

According to the coverage images of the three moments in each picture, AIPM's images move from west to east. There usually exists a large overlapping area but small discrepancy between adjacent images in a cover range. Over time, the region of AIPM's coverage on the entire hemisphere varies. On July 4th, 2016 and November 10th, 2016 at 23:00 to the 11th at 01:00, AIPM achieved complete coverage in the Northern Hemisphere and covered the Arctic region. On September 1st, 2016 and October 1st, 2016, both the Arctic and Antarctic regions were covered simultaneously. On October 30th, 2016 and November 29th, 2016, AIPM achieved complete coverage of the Southern Hemisphere and the Antarctic region. Thus, at certain moments, AIPM enables a complete observation at once of the Antarctic region or the Arctic region, which is beneficial for the study of polar areas.

The position of AIPM-images' latitude span, which is measured by every AIPM's coverage image, is changing with time, as shown in Fig. 7.

AIPM's coverage area moves from north to south, first covering the Arctic region (i.e., 67°N–90°N) then gradually covering the Antarctic region (i.e., 67°S–90°S), which is same as the sunlit areas' change law. This indicates that the location change of AIPM cover range is affected not only by Earth's rotation, but also by the sunlit area. During the simulation time, there are six minimum latitude spans peaks (Figs. 7(a)–7(f)). This is mainly because at this moment, the Earth is between the Moon and the Sun, resulting in an instantaneous decrease in the AIPM's coverage image. The maximum latitude span is 176°, during 19:00 on September 30th, 2016 to 16:00 on October 1st, 2016. Part of the time in the 1st–4th period can completely cover the Antarctic region, and part of the time in the last 3rd–6th period can completely cover the Arctic

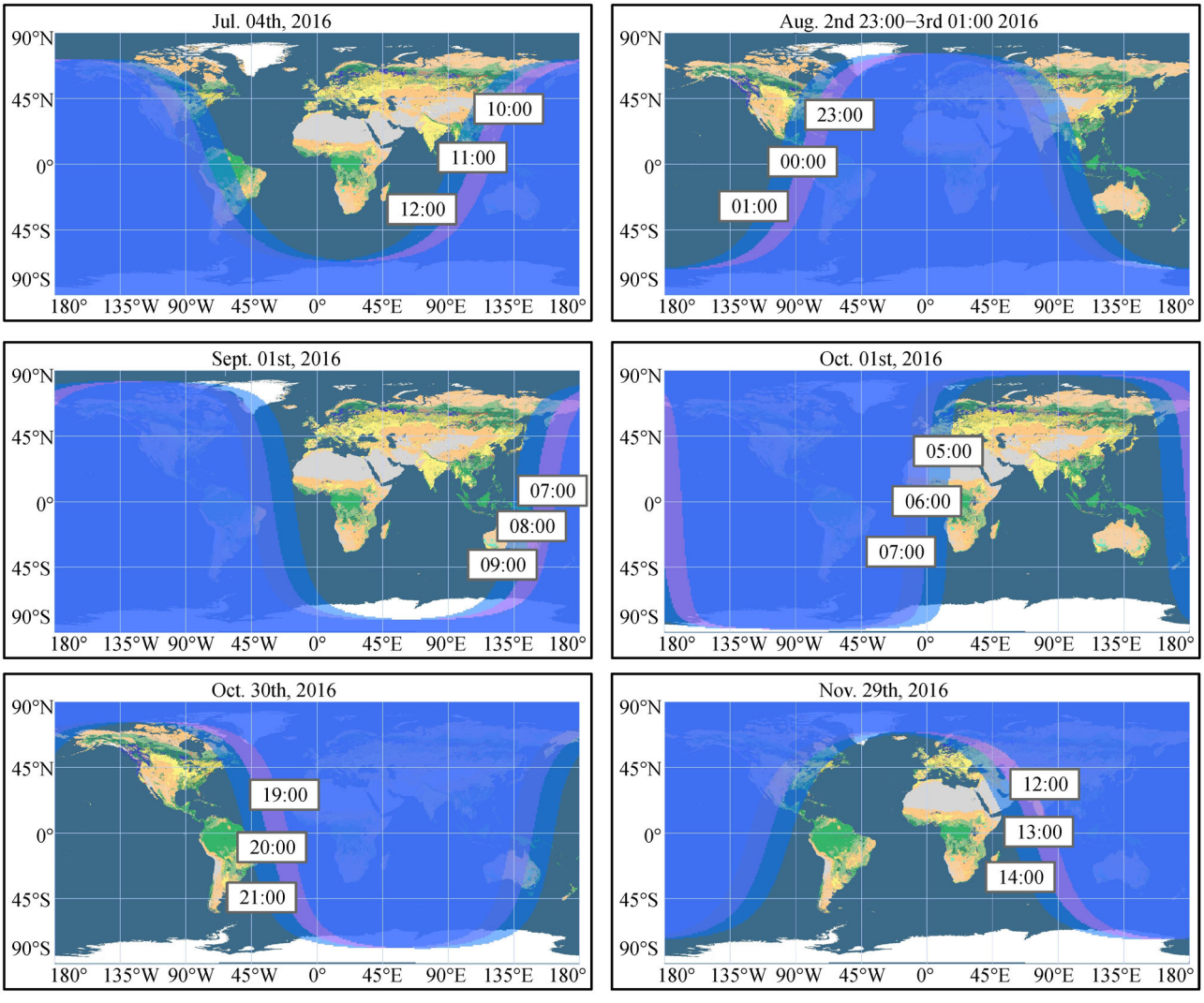

Fig. 6 AIPM's coverage images at six AIPM maximum coverage times. The white area denotes AIPM's cover area. The gradient blue shadow with time marked at the boundaries depicts different covered areas at different time.

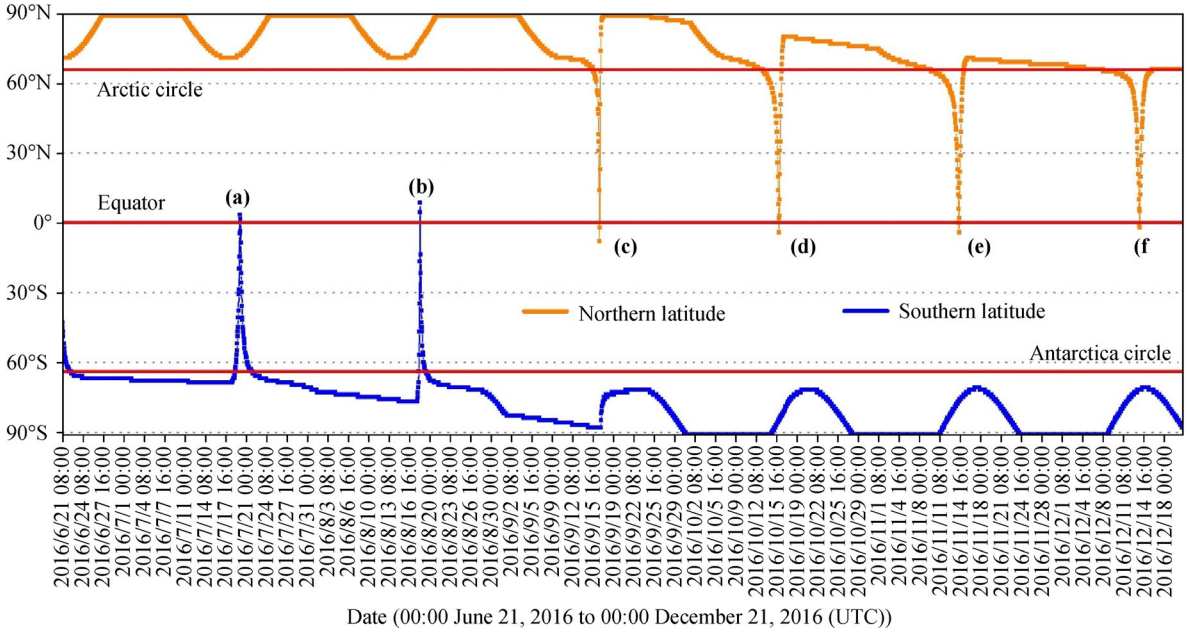

Fig. 7 Position change of AIPM coverage images' latitude span. The space between the orange and blue line depicts the zonal covered area by AIPM. We also mark the Arctic circle line (67°N), the Antarctica circle line (67°S) and the Equator line (red line).

region. The number of times that can cover the North Pole (90°N) and the South Pole (90°S) are 1164 and 1037, respectively, accounting for 26.36% and 23.48% of the experiment time. Therefore, AIPM can observe larger-scale instantaneous phenomenon in polar regions.

4.2 Coverage ability of GIPM

The variation curve of GIPM's coverage can be seen in Fig. 8.

Similar to AIPM's coverage, GIPM exhibits a cycle with 6 complete change periods. However, GIPM's coverage varies little and maintains a higher coverage; the minimum coverage is 72.22% (on December 13th, 2016), the maximum coverage is 98.89% (on September 30th, 2016), and the average coverage is 86.98%. The minimum coverage indicates that GIPM can stably cover more than 72.22% of the Earth's surface every day. Figure 8 also shows that GIPM's coverage increases in the first half of experiment to its peak and then decreases over time. This

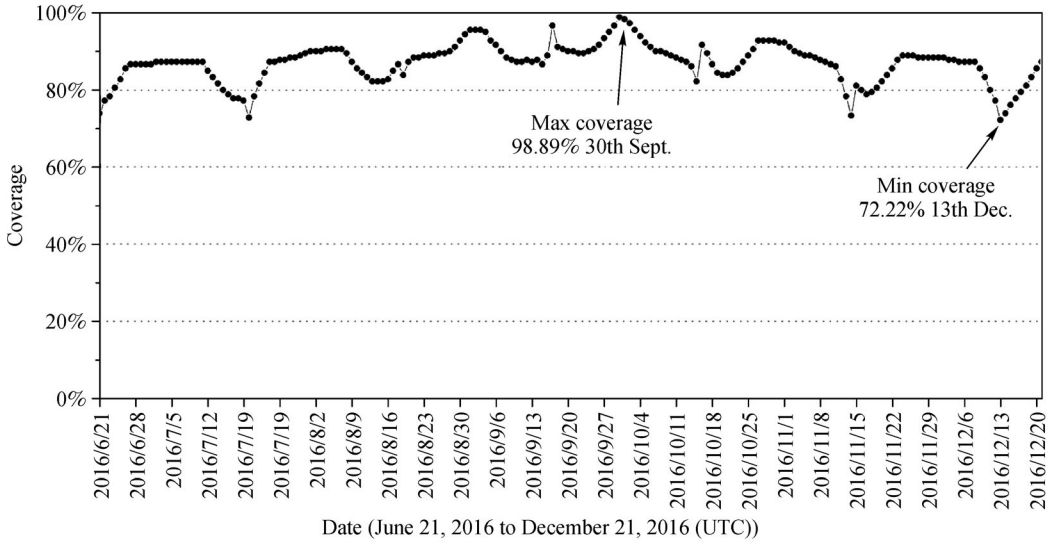

Fig. 8 Daily GIPM's coverage in experiment time. The curve line depicts the coverage at different times. The points on the picture depict the maximum and minimum coverages and their timings.

trend is caused by the GIPM imaging principle. When the subsolar point is near the tropic of Capricorn or Cancer, the polar region exhibits the "white night" phenomenon; GIPM can continuously observe the polar region during this time. As the subsolar point is near the equator, diurnal variation of the polar region is marked, and GIPM has no repeating observation area in the polar regions. In the middle of the experiment time, when the subsolar point reaches the equator, GIPM's coverage approaches its maximum. Therefore, the sunlit area affected GIPM's coverage.

Because the GIPM's coverage is relatively stable, we select its maximum coverage time of September 30th, 2016 and the minimum coverage time of December 13th, 2016 to map GIPM's coverage images in the Mercator projection coordinate system, as shown in Fig. 9.

At the time with maximum coverage (left picture in Fig. 9), GIPM can almost cover Earth's surface with the exception of the North pole. While at the time with minimum coverage (right picture in Fig. 9), GIPM cannot cover the Arctic and Antarctic regions. This provides further evidence that GIPM has a stable observing capability for most regions except for the north and south polar circles. Next, we will further analyze GIPM images in order to select a stable coverage area.

We measured the positions of GIPM's coverage images' latitude span.

Figure 10 indicates that the coverage image's latitude span of GIPM moves from north to south as a unit, which is the same as AIPM (Fig. 7). The maximum latitude span is 176°, on September 30th, 2016. As this graph shows, the area between 67°N and 67°S is relatively stable, which can form long-term continuous observational images using GIPM. This area contains a large part of the major continental areas and tropical areas, which are extremely sensitive to the ecological environment. Unlike the AIPM, there is no sudden change during GIPM's simulation time, which adds weight to the conclusion that GIPM's cover area is stable.

During the experiment time, the 1st–4th period of GIPM's coverage change can cover the North Pole, and the 4th–6th period of GIPM's coverage change can cover the

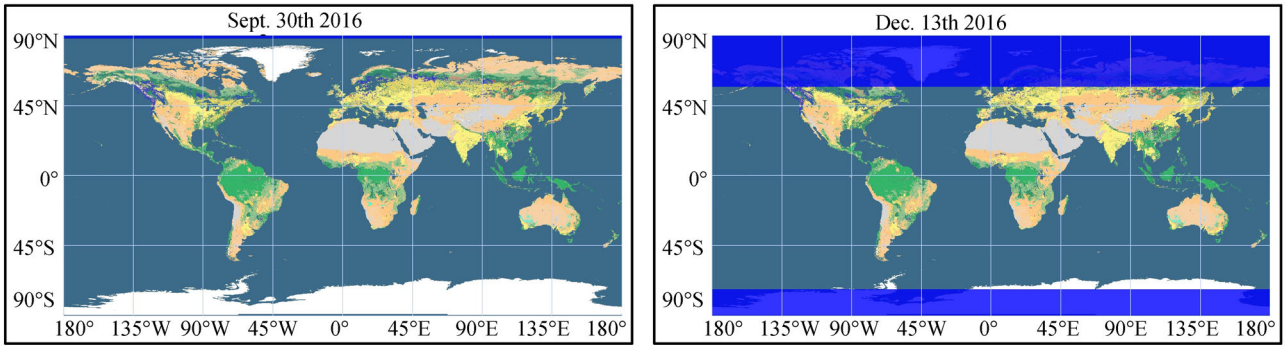

Fig. 9 GIPM's coverage images. The white area is GIPM's cover area. The blue area is the area that could not be covered.

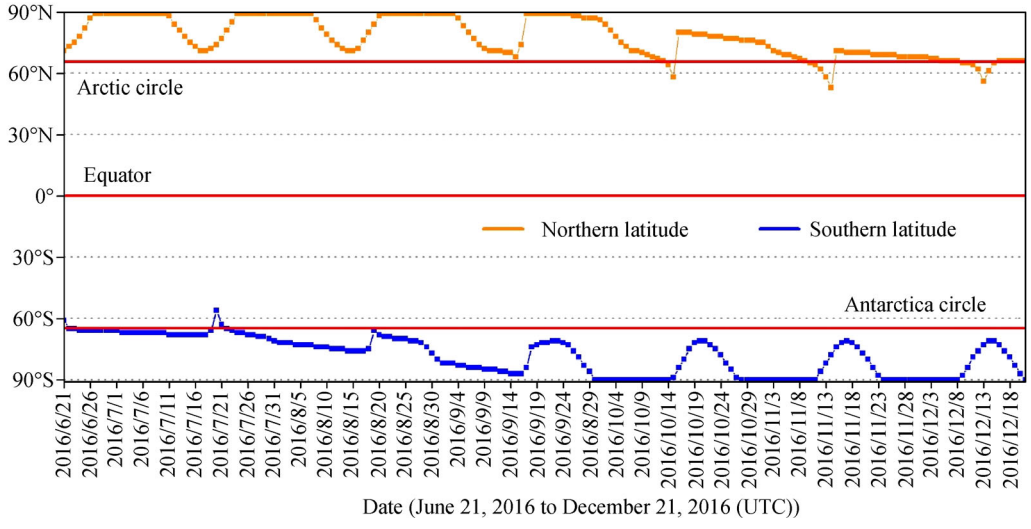

Fig. 10 Position change of GIPM's coverage images' latitude span. The area between the yellow and blue line depicts the area covered by GIPM. We also marked the Arctic circle (67°N), the Antarctica circle (67°S), and the Equator (red line).

South Pole. The duration of North Pole and South Pole coverage is 52 days and 46 days, respectively. In addition, the 3rd–5th period of GIPM's coverage change can cover parts of Antarctica and parts of the Arctic region simultaneously. This indicates that GIPM is useful for the study of the North and South Pole regions.

5 Discussion

5.1 Effectiveness of global image mosaicking method

Through the curve of the AIPM latitudinal range shown in Fig. 7, we found that the cover area of AIPM images varies considerably when AIPM's coverage reaches the minimum of each period. Therefore, whether GIPM's variation tendency in a long period will be affected significantly by the change of AIPM's coverage within a day need to be further researched. We selected July 5th, July 15th, and July 19th, 2016 as three experiment times when AIPM's coverage would reach its maximum, middle, and minimum, in order to compare AIPM's coverage images in one day (Pictures a, c, and e in Fig. 11) with GIPM coverage images at the same day (Pictures b, d, and f in Fig. 11).

As can be seen from the table above, the moment when AIPM's coverage reaches maximum (a) and middle (c), accumulated images could cover the whole of Earth's surface by splicing 24 AIPM's coverage images in one day with a coverage of 87.22% and 79.33%. GIPM's coverage images via global image mosaicking method has the same

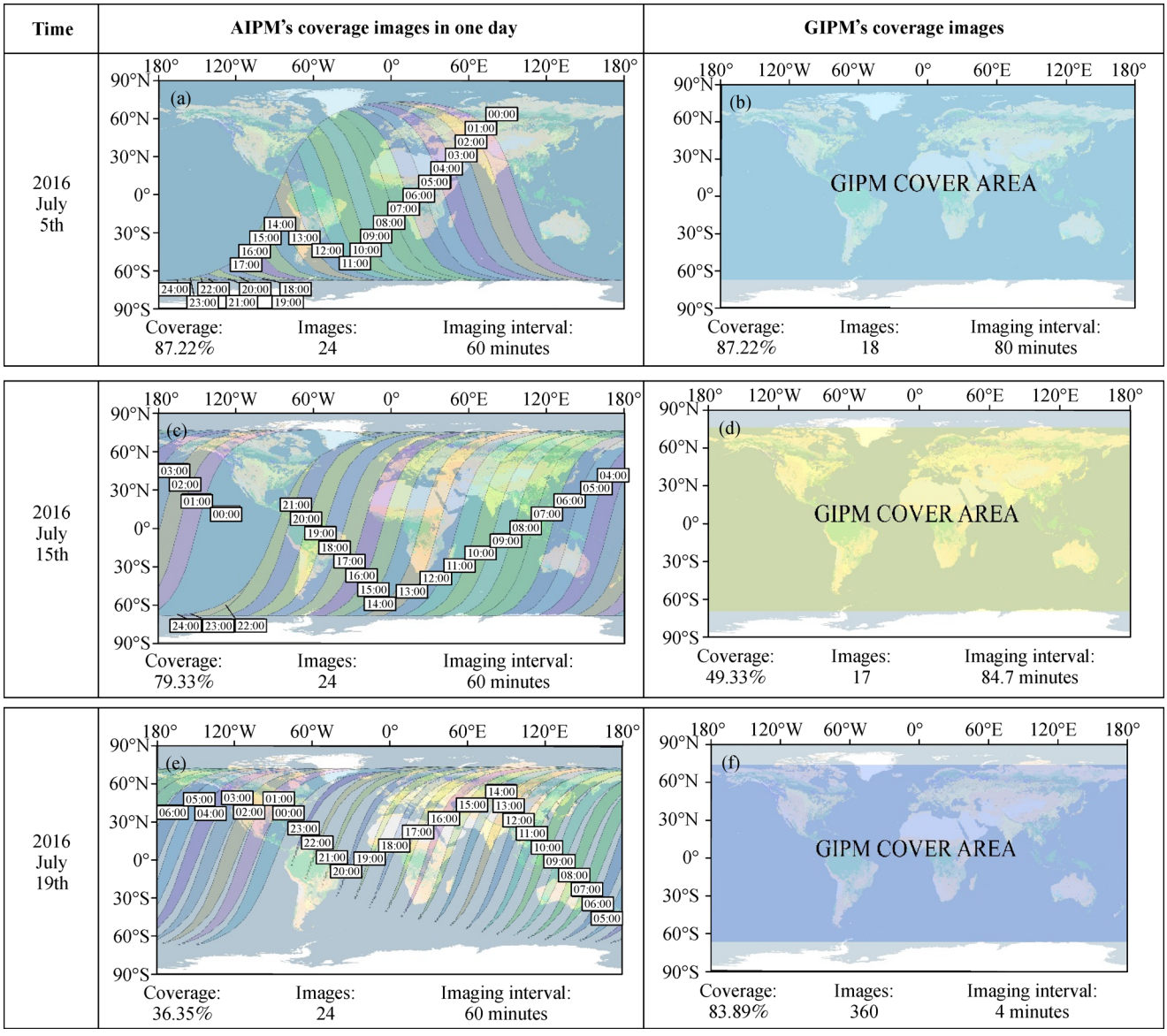

Fig. 11 Comparison of AIPM's coverage images and GIPM's coverage images. Pictures (a), (c), and (e) indicate AIPM cover areas at different times within one day. Hourly AIPM coverage images filled in with different colors with time marked at the boundaries. Pictures (b), (d), and (f) indicate GIPM cover area in one day

coverage range of AIPM in the same experiment time, but a lower imaging frequency of 18 times on July 5th, 2016 and 17 times on July 15th, 2016 in comparison with AIPM in the amount of 24 times in a corresponding day.

At the moment of AIPM's minimum coverage captured in Fig. 11(e), there are several obvious gaps distributed on the Earth surface; the spliced images of 24 AIPM images could not cover the whole Earth surface. Longitudinal extent on the same latitude of each AIPM's coverage image changes obviously on July 19th, 2016. Therefore, GIPM's coverage images via global image mosaicking method captured in f is wider than its real condition accumulated instantaneous observational images.

In conclusion, only if variation of AIPM's coverage is larger within one day, GIPM's coverage image cannot be accurately calculated by a global image mosaicking method. As can be seen from Fig. 7, this phenomenon happens only once a month. Therefore, the GIPM's variation tendency cannot be affected over a long period.

5.2 The inherent relation of AIPM's coverage and GIPM's imaging frequency

GIPM's imaging frequency f is negatively related to AIPM's cover area changing with time. Their inherent relation needs further studying to confirm. GIPM's imaging frequency f during the experiment time is exhibited as the black line shown in Fig. 12. Variation of AIPM's coverage (the same as Fig. 5), shown as the blue line, was combined into Fig. 12 under a unified time frame to show the relationship between them as an association.

As can be seen from the black line shown in the above figure, there are six change periods for GIPM's imaging frequency during the experiment time. The maximum of the imaging frequency f is 360 which is same as the radial pixel number of global Earth observation grids. The minimum value is 8, which is less than AIPM's imaging frequency which was set as 24 in this study. Statistics suggest that GIPM's imaging frequency less than 24 is 42.4% of the experiment time.

Combined with the variation curve of AIPM's coverage represented by the blue line in Fig. 12, it can be seen that GIPM's imaging frequency is anticorrelated with AIPM's coverage. The correlation index between them is -0.63. This reaches a remarkable degree. Therefore, GIPM's coverage images formed from AIPM's coverage images need a small frequency when AIPM's coverage reaches its maximum. It is effective for the global image mosaicking method to form GIPM's images on each day based on a single AIPM's image.

5.3 Potential applications

Previous studies found that the Moon-based Earth observation method has potential applications in the research of tripolar area, solid Earth dynamics, energy budget of Earth, and ocean internal waves (Guo et al., 2018). Based on the characteristics of two imaging processing methods, this paper mainly discusses AIPM and GIPM's applications in observation of the tripolar area and research of global albedo balance.

5.3.1 Tripolar coverage

Tripolar regions including the Antarctic range, Arctic region, and Tibet Plateau, characterized by large spatial scale and extreme sensitivity to global environment changes, need long-term integral observation (Gao, 2012; Dong and Zou, 2014; Jueterbock et al., 2016). Based on the analysis in Section 4, AIPM can provide a large spatial coverage observation at once while GIPM can provide stable observational region over a long time period.

In order to analyze AIPM and GIPM's performance in observation of tripolar areas, AIPM and GIPM's coverage images generated in this paper are superimposed onto tripolar regions (Arctic range: NSIDC, https://nsidc.org/) to calculate temporal coverage under four different spatial coverages of 100%, larger than 80%, larger than 50%, and larger than 0%. The results are shown in Table 1.

We can see from Table 1, in the case of spatial coverage

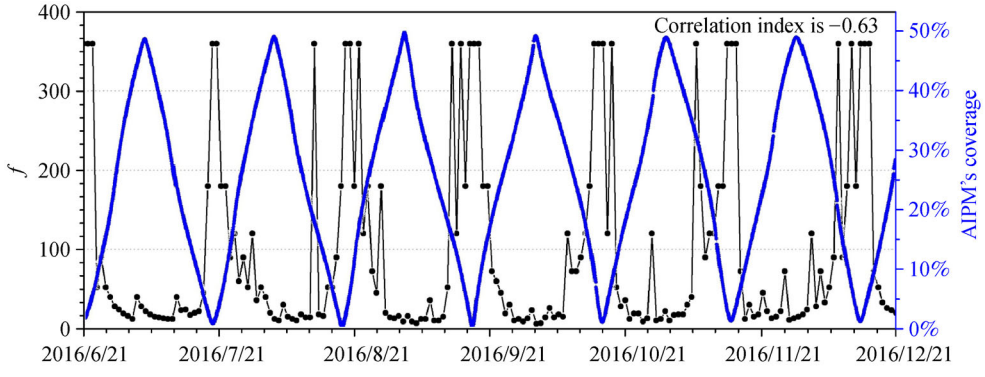

Fig. 12 Relationship between GIPM's imaging frequency and AIPM's coverage. The black line is GIPM's imaging frequency. The blue line is AIPM's coverage.

Table 1 Temporal coverage of AIPM and GIPM for different spatial coverages in the tripolar regions

Global Spatial coverage	Yearly temporal coverage							
	Arctic Region		Tibet Plateau		Antarctic Region		Tripolar regions Simultaneity	
	AIPM	GIPM	AIPM	GIPM	AIPM	GIPM	AIPM	GIPM
100%	2.92%	28.26%	15.99%	100%	3.08%	25.00%	0	0
> 80%	14.31%	34.24%	20.52%	100%	15.31%	29.35%	0	1.10%
> 50%	22.40%	39.67%	24.86%	100%	23.14%	42.39%	0	6.50%
> 0%	88.93%	100%	35.48%	100%	70.95%	98.36%	23.89%	98.36%

of 100%, that AIPM and GIPM can both cover a single polar region completely at certain times, which is vital to study transient variation geoscience phenomenon of polar regions. In other cases of spatial coverage, GIPM's coverage is larger than AIPM for a single polar region, and GIPM can cover the Tibet Plateau area completely in a whole year. In addition, AIPM can observe parts of tripolar regions simultaneously in at least 23.89% of a year, which is significant for the study of linkage relationship of the tripolar regions. GIPM can realize synchronized observed parts of tripolar regions for at least 98.36% of a year, which can provide a long-term continuous observation for the study of tripolar regions as whole.

5.3.2 Earth's albedo

Earth radiation balance, which global climate change depends on, affects the ecological environment of the Earth (Smith et al., 2009; Hansen et al, 2011; Stephens et al., 2015; Dewitte and Nevens, 2016). Voigt et al. (2013) found that reflection energy is distributed and balanced in the northern and southern hemispheres by analyzed TOA irradiances data as measured by Clouds and the Earth's Radiant Energy System- Energy Balanced and Filled (CERES-EBAF) in 2000-10.

GIPM can provide a long-term continuous observation between 67°N and 67°S, which is advantageous in the study of Earth radiation balance. Based on the study of Voigt et al. (2013), we repeat his scientific research ideas in the study of TOA albedo, which can reflect the comprehensive changes in surface and atmosphere, to find some special phenomenon from the perspective of the Moon-based platform.

Assuming no changes in scene properties in one day (Loeb et al., 2007), GIPM can be applied to obtain TOA albedo, which is similar to albedo daily production of CERES- SYN data (Synoptic TOA and surface fluxes and clouds). We average TOA albedo data from SYN1deg data (Synoptic TOA and surface fluxes and clouds, https://ceres.larc.nasa.gov/), the spatial resolution of which is 1°, the same as global observation grids in this study, measured by CERES-SYN in 2006-17. The resultant image is shown in Fig. 13.

When we superimpose the GIPM stable observational range (67°N–67°S) onto the above data to calculate albedo's average value of two equal areas (0–67°N and 0–67°S), an interesting phenomenon appeared. The global albedo average value is the same in these two areas. Hence, we define 67°N/67°S as the albedo balance line of the northern and southern hemispheres. We further use SYN1deg data to calculate the position of the albedo balance line in inter-annual scale. The results are shown in the following Fig. 14.

As can be seen from the above figure, the latitude of albedo balance line moves between 65°N/S and 68°N/S with uncertain changes, which is the dominant cover area of GIPM. The factors that influence the changes are complex and diverse, such as Earth surface, polar ice cover, solar radiation, extreme weather, etc. Some of these factors are characterized by large-scale in space and long-

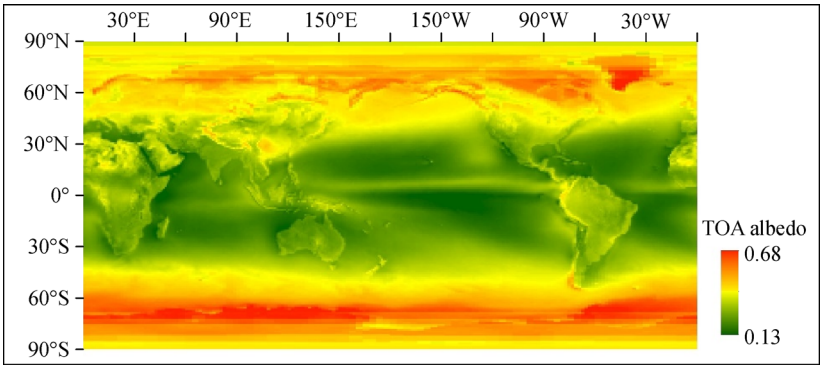

Fig. 13 Mean value of TOA albedo in 2006–2017.

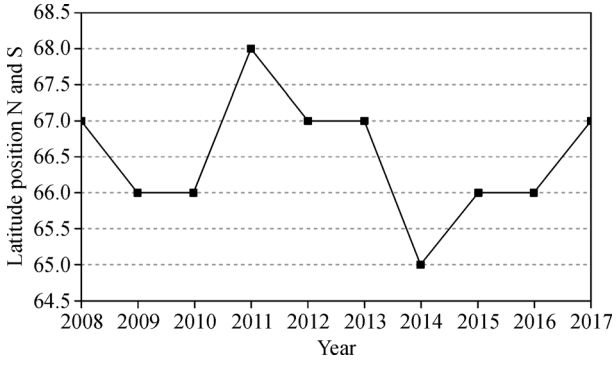

Fig. 14 Position of the albedo balance line annually.

term in time, which need to be monitored in a long-term period by GIPM.

Therefore, GIPM can help to clarify mechanism of the changes of global TOA albedo balance line, which can provide support for the study of global energy balance and multi-layer linkage effect.

6 Conclusions

In consideration of the demand for global change study by the Moon-based method, this paper proposes AIPM and GIPM for the Moon-based platform's optical sensor, and analyzed their coverage ability by simulated coverage images through the Moon–Sun elevation angle model and Global image mosaic method. Results show that AIPM has the ability of instantaneous large-range observation which can cover nearly half of Earth at a certain time. AIPM is helpful for the study of large-scale geoscience phenomenon in an instant time and the study of tripolar regions. GIPM can stably observe 67°N–67°S of the Earth every day, which is useful for the study of global change over a long-term period.

Through simulating coverage images of AIPM and GIPM, we found that AIPM's coverage has a regularly change between 0%–50% with a period of 29.5 days which is the same as the Moon's revolution. At a specific moment, AIPM can completely cover the whole Antarctic or Arctic region instantaneously. GIPM also has a period of 29.5 days. Its maximum and minimum coverage are 89% and 79%, respectively. GIPM enables stable daily coverage of 67°N–67°S. AIPM's coverage is affected by the Moon's revolution and its cover area is affected by the Earth's rotation and sunlit area. GIPM's coverage and cover area are all affected by sunlit area.

This study also found that the global image mosaicking method can effectively obtain GIPM's cover images for the study of global change in a long-term period. GIPM's imaging frequency is anticorrelated with AIPM's coverage with a correlation index of −0.63. AIPM and GIPM have great advantages for observation of Earth's tripolar regions. From the perspective of GIPM, we have verified that there is a balance line of TOA albedo.

The result of this study indicates that AIPM and GIPM play a significant role in linking observations acquired from the Moon-based platform to global change. In the future, more applications could be examined with AIPM and GIPM in great detail.

Acknowledgements This research was supported by the National Natural Science Foundation of China (Grant No. 41590853) and the Key Research Program of Frontier Sciences of Chinese Academy of Sciences (Grant No. QYZDY-SSW-DQC026). We also thanks NASA Jet Propulsion Laboratory for providing the free ephemeris data.

References

Butler D (2014). Earth observation enters next phase. Nature, 508(7495): 160–161

Carruthers G R, Page T (1972). Apollo 16 far-ultraviolet camera/spectrograph: earth observations. Science, 177(4051): 788–791

Chuvieco E, Li J, Yang X (2010). Advances in earth observation of global change. Springer Netherlands, 35(6): 463–483

Civicioglu P (2012). Transforming geocentric cartesian coordinates to geodetic coordinates by using differential search algorithm. Comput Geosci, 46(3): 229–247

Clarke A E, Roy D (2003). Astronomy Principles and Practice (PDF) (4th ed). Bristol: Institute of Physics Pub. p. 59.

Cui K, Xiang J, Zhang Y (2017). Mission planning optimization of video satellite for ground multi-object staring imaging. Advances in Space Research, 2017, 61(6): 1476–1489

Dewitte S, Nevens S (2016). The total solar irradiance climate data record. Astrophys J, 830(1): 25

Ding Y, Guo H, Liu G (2014). Coverage performance analysis of earth observation from lunar base for global change detection. Journal of Hunan University, 41(10): 96–102 (in Chinese)

Dong H, Zou X (2014). Variations of sea ice in the antarctic and arctic from 1997–2006. Front Earth Sci, 8(3): 385–392

Folkner W M, Williams J G, Boggs D H, Park R S, Kuchynka P (2014). The planetary and lunar ephemerides de430 and de431. IPN Progress Report, 196: 1–81

Gao D Y (2012). Global warming and ecology environment change in the three poles of Earth. Chinese Journal of Nature, 34(1): 18–23 (in Chinese)

Guo H, Fu W, Li X, Cen P, Liu G, Li Z, Wang C, Dong Q, Lei L, Bai L, Liu Q (2014). Research on global change scientific satellites. Sci China Earth Sci, 57(2): 204–215 (in Chinese)

Guo H D (2009). Space-based observation for sensitive factors of global change. Bulletin of the Chinese Academy of Sciences, 23(4): 226–228 (in Chinese)

Guo H D, Ding Y X, Liu G, Zhang D W, Fu W X, Zhang L (2014). Conceptual study of lunar-based SAR for global change monitoring. Sci China Earth Sci, 57(8): 1771–1779

Guo H D, Liu G, Ding Y X (2018). Moon-based earth observation: scientific concept and potential applications. Int J Digit Earth, 11(6): 546–557

Guo H D, Zhu L W (2013). Earth observation for global change sensitive variables: mechanisms and methodologie. Bulletin of the Chinese Academy of Sciences, (4): 525–530

Hansen J, Sato M, Kharecha P, von Schuckmann K (2011). Earth energy imbalance and implications. Atmos Chem Phys, 11(9): 27031–27105

Huang S (2008). Surface temperatures at the nearside of the Moon as a record of the radiation budget of Earth climate system. Adv Space Res, 41(11): 1853–1860

Jueterbock A, Smolina I, Coyer J A, Hoarau G (2016). The fate of the arctic seaweed fucus distichus under climate change: an ecological niche modeling approach. Ecol Evol, 6(6): 1712–1724

Karalidi T, Stam D M, Snik F, Bagnulo S, Sparks W B, Keller C U (2012). Observing the earth as an exoplanet with loupe, the lunar observatory for unresolved polarimetry of earth. Planet Space Sci, 74(1): 202–207

Ligas M, Banasik P (2011). Conversion between cartesian and geodetic coordinates on a rotational ellipsoid by solving a system of nonlinear equations. Geodesy and Cartography, 60(2): 145–159

Liu G, Guo H D, Wang X Y, Zhang L (2016). Report on the Scheme and Key Technologies of Lunar Base Earth Observation. Strategic Pioneer Program on Space Science of Chinese Academy of Science

Loeb N G, Wielicki B A, Rose F G, Doelling D R (2007). Variability in global top-of-atmosphere shortwave radiation between 2000 and 2005. Geophys Res Lett, 34(3): L03704

Mouroulis P, Green R O, Chrien T G (2000). Design of pushbroom imaging spectrometers for optimum recovery of spectroscopic and spatial information. Appl Opt, 39(13): 2210–2220

Nie C W, Liao J J, Shen G Z, Duan W T (2018). Simulation of the land surface temperature from moon-based earth observations. Adv Space Res, doi: 10.1016/j.asr.2018.09.041

Pallé E, Goode P R (2009). The lunar terrestrial observatory: observing the earth using photometers on the Moon's surface. Adv Space Res, 43(7): 1083–1089

Petit G, Luzum B (2010). IERS conventions (2010). IERS Technical Notes, 36: 1–95

Ren Y Z, Guo H D, Liu G, Ye H L (2017). Simulation study of geometric characteristics and coverage for Moon-based Earth observation in the electro-optical region. IEEE J Sel Top Appl Earth Obs Remote Sens, 10(6): 2431–2440

Schombert J (2011). Earth Coordinate System. University of Oregon Department of Physics.

Smith W K, Gao W, Steltzer H (2009). Current and future impacts of ultraviolet radiation on the terrestrial carbon balance. Front Earth Sci China, 3(1): 34–41

Stephens G L, O'Brien D, Webster P J, Pilewski P, Kato S, Li J (2015). The albedo of Earth. Rev Geophys, 53(1): 141–163

Tsukamoto A, Kamisaka W, Senda H, Niisoe N, Aoki H, Otagaki T (1996). High sensitivity pixel technology for a 1/4-inch PAL 430 k pixel IT-CCD. In: Proceedings of IEEE Custom Integrated Circuits Conference

Voigt A, Stevens B, Bader J, Mauritsen T (2013). The observed hemispheric symmetry in reflected shortwave irradiance. J Clim, 26(2): 468–477

Wild M (2009). Global environmental change. J Geophys Res D Atmospheres, 114(11): D00D16

Wu J (1999). Hierarchy and scaling: extrapolating information along a scaling ladder. Can J Rem Sens, 25(4): 367–380

Xu Z, Chen K S (2018). On signal modeling of Moon-based synthetic aperture radar (SAR) imaging of earth. Remote Sens, 10(3): 486

Ye H L, Guo H D, Liu G, Ren Y Z (2017). Observation scope and spatial coverage analysis for earth observation from a Moon-based platform. Int J Remote Sens: 1–25

Ye H L, Guo H D, Liu G, Ren Y Z (2018). Observation duration analysis for Earth surface features from a Moon-based platform. Adv Space Res, 62(2): 274–287

Zhang D W (2012). Study on methodology of lunar-based Earth observation for global change. Dissertation for the Master Degree. Shanghai: East China Normal University (in Chinese)

Zhu C, Xie Zh, Li F (2012). An Introduction to Global Change Science (3rd ed). Beijing: Science Press (in Chinese)